



## Simulation of Thermosyphon Rankine Engine

Muhamad Fauzi Othman<sup>1</sup>, Muhammad Fairuz Remeli<sup>1\*</sup>, Nur Adilah Azizi<sup>1</sup>, Baljit Singh<sup>1</sup>

<sup>1</sup> School of Mechanical Engineering, College of Engineering, Universiti Teknologi MARA Shah Alam, Selangor, Malaysia

### ABSTRACT

The increasing global energy demand has led to other alternative ways of harvesting energy from renewable resources. This energy cause less environmental pollution and deterioration of humans' health. Thermosyphon Rankine engine (TSR) is a concept used for direct electrical power generation from low-grade heat sources. In this project, an extended investigation on previous experimental done was conducted through a simulation approach using Computational Fluid Dynamic (CFD) analysis to simulate a two-phase flow, phase change occurred during evaporation and condensation processes inside the thermosyphon under different power inputs of 245 W, 552 W, and 984 W. Also the water was used as a working fluid. The volume of fluid (VOF) technique was used to model the phase change using ANSYS FLUENT software. The simulation investigated temperature profile, water volume fraction, and velocity. Then, CFD predicted temperature profile was compared with the previous experimental data, and percentage error was calculated. Compared to the experimental one, CFD predicted temperature profile was higher than the experimental one due to mechanical losses during experimentation. Meanwhile, the model managed to simulate vapor bubbles and nucleate boiling during phase change. It showed that the VOF model with the in-built evaporation-condensation model developed by Lee only simulated nucleate boiling at the interphase between water and vapor phase during evaporation and condensation processes.

#### Keywords:

Thermosyphon; Rankine cycle; CFD;  
VOF; Evaporation

Received: 12 June 2022

Revised: 31 August 2022

Accepted: 4 Sept 2022

Published: 19 October 2022

### 1. Introduction

As the world's technology and industrial operations evolve, the demand for energy resources has increased to keep up with this progress [1]. Due to population and economic growth, it is expected that global energy demand would double by 2050 [2]. Fossil fuels are the most widely used energy resource globally, accounting for more than 80% of current primary energy use. However, due to increased demand, fossil fuel reserves will be depleted in the next century, resulting in energy resource shortages. However, some contend that the use of fossil fuels contributes to global pollution and the degradation of human health [3]. Aside from that, the usage of fossil fuels contributes to greenhouse gas (GHG) and pollution emissions in the environment [1]. From here, renewable energy had been taken as an option in making strategies for sustainable development. These strategies involve three significant technological changes, energy savings on the demand side, efficiency

\* Corresponding author.

E-mail address: fairuz1299@uitm.edu.my

<https://doi.org/10.37934/araset.28.2.102123>

improvement in energy production, and replacement of fossil fuels by various sources or renewable energy [4].

Encouraging the use of renewable energy led to many studies related to energy harvesting using renewable energy sources. One of them is the use of heat pipes in conjunction with renewable energy sources, including solar, waste heat, geothermal energy, the heat produced by solar collectors, and waste heat utilization for electrical power generation. TSR (Thermosyphon Rankine Engine) is a novel concept for generating electricity from low-grade heat sources. This engine is a modified version of a heat pipe, with a turbine added between the adiabatic and condenser section of the thermosyphon to improve the system's heat and mass transmission properties, making the system a Rankine Cycle Engine. In other words, TSR is an environmentally beneficial technology for direct electrical power extraction from low enthalpy heat sources (particularly less than 100°C since the interior air system has been evacuated) [5].

The system works when heat is supplied into a thermosyphon through the bottom section (evaporator section), where a liquid pool exists, converting the working fluid to vapour. The vapour rises through the tube's middle section (adiabatic section) and ascends to the top (condenser section). The vapour condenses in the condenser section and transfers its latent heat of vaporization to the condenser wall, converting the vapor back to a liquid state. In contrast to a heat pipe, which depends on capillary forces to return the liquid, the thermosyphon uses gravity or centrifugal forces to return the condensed liquid to the evaporator.

A temperature difference drives any mechanism of heat transmission. According to fundamental heat transfer theory, the wider the temperature difference, the faster the heat transfer rate. The thermosyphon's heat transfer performance is influenced by a variety of factors, including the working fluid's thermophysical properties, the thermosyphon's geometry, and orientation, the gravity field, and the operating temperature or pressure. The selection of working fluid influences the system because it determines the heat pipe's thermal performance [5]. Hence, several models had been experimented with in the previous studies to increase the system's efficiency.

### *1.1 Experimental work on thermosyphon Rankine Engine*

In prior research, experimental work on a thermosyphon Rankine engine was carried out to analyze and investigate how various factors and operating conditions affect the system's performance and efficiency. However, few studies looked directly at the thermosyphon Rankine engine, instead of focusing on the performance and output of the thermosyphon under various conditions, such as working fluid type, fill ratio (FR), inclination angle, and power input.

Elshamy [6] performed experimental research on the performance of the thermosyphon Rankine engine as a low-temperature heat engine. From the experiment, temperature variation with dimensionless distance for different input power and output power with input power was recorded. The temperature of the thermosyphon at applied input power is greater at the evaporator section than in the condenser section as steam moves away from the evaporator section to the condenser section due to temperature decrease. He also stated that as evacuation pressure is applied to the system, it reduces the boiling temperature. This option was good as lower power was needed to boil the water. The experiment also shows that as the input power increase, the all-temperature gradient and the output power also increase. However, the TSR's efficiency decrease as the output power increases due to the mechanical losses.

Habieeb *et al.*, [7] presented experimental work to study the temperature distribution along the TSR and the effect of filling ratio, turbine exit area, and cooling water flow rate on both turbine rotational speed and exit power, using water as working fluid. The experiment consists of a

galvanized steel tube, an electric heater, a constant head tank, a turbine and rotor based on the Hero reaction turbine principle, and measurement devices. The results obtained showed that the optimum filling ratio was approximately 13.6%, and the output power increases as the condenser cooling water flow rate increases. Also, the maximum output power is produced at the minimum area ratio, but the optimum turbine rotational speed at an area ratio of 3.1%.

The improved design of TSR was designed by Ziapour [8]. He states that in a simple TSR system consisting of a single tube, thermal performance is restricted by entrainment and flooding phenomena. The flooding phenomena can be solved by using a loop-type TSR system where vapor and liquid flow passages are separated [8]. Hence, Ziapour developed a looped type TSR system where vapor and liquid flow passage are separated by installing a liquid feeding tube with a showering nozzle using an impulse turbine. The improvements made to the loop TRC system are by using the added superheating processes, a steam drum-type evaporator for receiving the renewable energy needed via the flow boiling process, and a convergent-divergent nozzle to provide the supersonic vapor flow for the blades of the impulse turbine after the superheating process. This design managed to increase the efficiency of the TSR system by 0.78 %.

Most of the TSR is applied and connected to the Organic Rankine Cycle (ORC). Recently, Saadon *et al.*, conducted analytical and simulation studies of the Organic Rankine Cycle (ORC) system using MATLAB and REFPROP for two different system configurations. They found that the best thermal efficiency of the ORC is the design using a superheater rather than using a preheater. The superheater paired with a turbofan engine produced a lower thrust specific fuel consumption (TSFC) compared to the preheater. The study concluded that the ORC system has a big potential for recovering waste heat from an aircraft engine [9][10].

Rabah *et al.*, performed the energy and exergy studies of a combine ORC and a vapor compression cooling system. Three organics working fluids were selected including R123 (isentropic), R134a (wet) and R600 (dry). Using parametric analysis, they found that the R123 produced the highest thermal and exergy efficiency with 52% and 25%, respectively. They also found that exergy was significantly destroyed in condenser and ORC evaporator [11].

## 1.2 Modelling and simulation on Thermosyphon

Modelling and simulation have been widely utilized to improve the design and predict the system's performance under consideration. In the thermosyphon Rankine engine case, most simulations focus only on the thermosyphon's thermal properties. Most of the thermosyphon research has employed computational fluid dynamic (CFD) analysis to analyze the device's thermal characteristics and performance under various conditions and variables. These analyses were carried out to better understand the complex multiphase heat and mass transfer characteristics, the variations in temperature profiles, and the system's performance and efficiency when subjected to various variables and operating conditions.

Alizadehdakhel *et al.*, [12] conducted two dimensional CFD analysis using FLUENT™ version 6.2. where this CFD package was used to model the gas-liquid and complex heat and mass transfer, encountered phase change during evaporation and condensation inside the thermosyphon under different operating conditions. The CFD results will be compared to experimental measurements better to understand the differences in temperature profiles and thermosyphon performance. In their study on CFD simulation of flow and heat transfer in a thermosyphon, Yang *et al.*, [13] discovered that CFD analysis utilizing UDF in FLUENT could simulate thermal properties and phase change in the evaporation and condensation sections of the thermosyphon.

Fadhl *et al.*, [14] created a comprehensive CFD model in ANSYS FLUENT utilizing VOF (volume fraction equation) and UDFs to simulate the dynamics of two-phase flow and heat transfer processes in thermosyphons using water as the working fluid. In addition, Fadhl *et al.*, [15] also investigated the use of CFD modelling to simulate two-phase heat transfer processes during thermosyphon start-up and steady-state operation utilizing R134a and R404a as working fluids instead of water. This study also simulated the pool boiling in the evaporator section and liquid film in the condenser section using the CFD model.

Fertahi [16] used a two-phase volume of fluids (VOF) model to build a comprehensive computational fluid dynamics (CFD) model to analyze pool boiling in the evaporator section and liquid film condensation in a closed thermosyphon. The findings were analyzed in terms of vapour volume fraction change, temperature, and vertical velocity at various points along the thermosyphon.

Hussam *et al.*, [17] conducted simulation works on geyser boiling in a two-phase thermosyphon using three-dimensional CFD modelling which was also developed using UDFs and VOF (volume fraction equation) methods. In this study, water and refrigerant R134a are used as working fluids. The CFD model was able to simulate the complex multiphase heat and mass transfer characteristics of the boiling and condensation in the thermosyphon, heat transfer characteristics of the cooling fluid in the condenser and pool boiling behaviour for different working fluids and for the first time, CFD simulation has success in predicted a flow pattern that takes place with water at low power throughput, which known as geyser boiling.

Wang [18] also studied geyser boiling in a two-phase closed thermosyphon, but with using a combined CFD and visualization method to simulate the heat transfer behaviour during geyser boiling based on improved and original Lee model. The CFD model was created using the Lee model of phase change's VOF technique, and visualisation was done by observing the experimental works. The enhanced Lee model, on the other hand, focuses on considering superheat to improve performance. The upgraded model outperforms the old model in terms of prediction accuracy.

Simulation is done using a combined method of CFD and visualization also being carried out by Yinfeng Wang *et al.*, [19], where the CFD model was developed using the volume of fluid (VOF) to investigate the heat and mass transfer and performance through a range of filling ration and flow regime. The simulation found that the flow regime changes from smooth unidirectional flow to geyser oscillation flow by increasing the filling ratio. Results show that the same two-phase flow regimes predicted, and measured temperatures and thermal resistances deviated by less than 9%.

Temimy [20] performed a CFD modeling study to investigate the flow and heat transfer in a closed thermosyphon heat pipe. The volume of the fluid model (VOF) was implemented in Fluent. The simulation was to clear out the behaviour of the rising hot steam and the downward condensate flows near the inner pipe wall. Due to both phases are facing each other near the wall, the high momentum phase continues its flow in its way and shifts the other phase from the wall. Thus, the flow behaviour leads the steam and condensate to flow in an unstable spatial flow upward and downward, respectively. The flow continues even when a steady state is achieved and creates a secondary mass and heat transfer between the phases.

Hence, in this study, an extended investigation from Elshamy [6] experimental is performed using the CFD simulation approach of the Volume of Fluid (VOF) method to analyze the two-phase flow and phase change that occurred inside the system during evaporation and condensation processes using different power inputs.

## 2. Methodology

This paper conducted an extended investigation using a simulation approach based on the thermosyphon Rankine engine model used by Elshamy [6] in his experimental work. Due to a lack of information about the turbine utilized in the experiment, the simulation was limited to the thermosyphon operation. The software ANSYS FLUENT student version 2020 R2 was employed for this investigation.

### 2.1 Geometry model

For this study, the 2D geometry of the thermosyphon model was created in Design Modeler. 2D geometry was used to reduce the computational time for the simulation and it was simpler compared to using 3D geometry. The thermosyphon model consisted of an evaporator section, adiabatic section, condenser section, two nozzles and two returning pipes. Based on Elshamy [6] model, the total length of thermosyphon, outer diameter and inner diameter were 1.4 m, 0.21 m and 0.195 m, respectively. The length of the evaporator, adiabatic, condenser section, the diameter of nozzles and returning pipes were tabulated in Table 1.

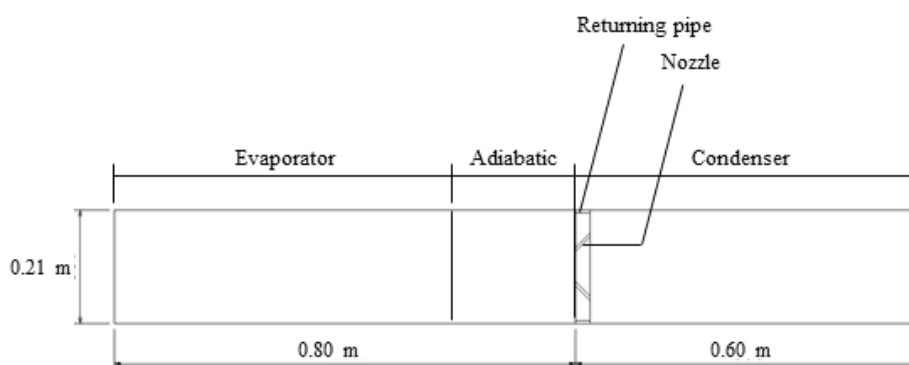


Fig. 1. Schematic diagram of TSR model

Table 1

Specification of TSR model [6]

Part	Dimension (m)
Outer diameter	0.21
Inner diameter	0.195
Length of the evaporator section	0.6
Length of adiabatic section	0.2
Length of condenser	0.6
Diameter of nozzle	0.007
Diameter of returning pipe	0.005

### 2.2 Mesh

For this study, the meshing for this model was created as shown in Figure 2, the model was set to an element size of 0.004 m. Then, near the right and left walls of the thermosyphon, the inflation method was selected. The inflation [10, 15] was set with 10 layers with a total thickness option of a growth rate factor of 1.2 and a maximum thickness of 0.01 m. At the nozzles, edge sizing was selected with divisions of 15. For finer meshing, multizone of Quad/Tri method and face meshing was applied. As a result, elements of 50 776 with nodes of 29 344 were created.

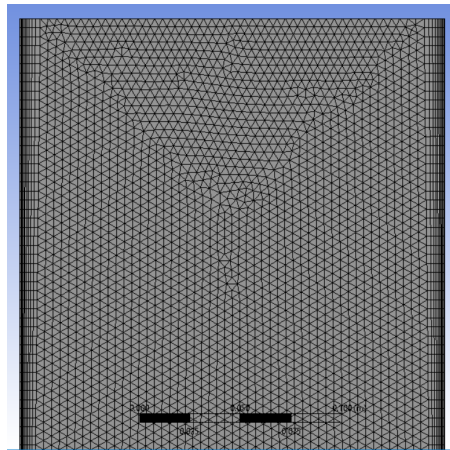


Fig. 2. Close-up of mesh structure at the condenser section

### 2.3 Material condition

In the material section, air, water (liquid) and water (vapor) were selected for fluid, while copper was added as material for the solid wall [6].

**Table 2**

Material properties for fluid [21]

Material	Density (kg/m <sup>3</sup> )	Thermal capacity (J/kg.K)	Thermal conductivity (W/m.K)	Dynamic viscosity (kg/m.s)	Molar mass (kg/k.mol)	Enthalpy (J/kg.mol)	Reference temperature (K)
Air	1.225	1006.43	0.0224	$1.7892 \times 10^{-5}$	28.966	0	298.15
Water (liquid)	1000	4182	0.6	$9.00 \times 10^{-4}$	18.0152	0	298.15
Water (vapor)	0.5542	2014	0.0261	$1.34 \times 10^{-5}$	18.01534	$2.292325 \times 10^7$	298.15

**Table 3**

Material properties for solid [6]

Material	Density (kg/m <sup>3</sup> )	Thermal capacity (J/kg.K)	Thermal conductivity (W/m.K)
Copper	8978	381	387.6

### 2.4 Numerical Modelling

Numerical solutions based on the finite volume approach are more complex than single-phase flows for multiphase flows. The difficulties arise because the interfaces between the phases are not stable, and physical characteristics such as density and viscosity fluctuate at the interfaces between the distinct phases, necessitating a significant computational effort. As a result, the volume of fluid (VOF) approach was utilized to solve these difficulties by calculating the motion of all phases and implicitly defining the motion of the interfaces from this result [17].

The ANSYS Fluent CFD solver was used with the Volume-of-Fluid (VOF) approach to describe the complex multiphase flow between gas and liquid. The VOF method [20] is based on the assumption that two or more phases are not interpenetrating, and the volume fraction of each new phase must be included in the computation for each additional phase. The VOF approach benefits from using only one set of momentum equations and tracking the interfaces between fluid phases [22]. In the VOF method, each cell should be filled with at least one fluid and accordingly, three

possible conditions arise; cell with  $\alpha = 0$  is occupied by vapor, the cell with  $\alpha = 1$  is full of liquid and cell with  $0 < \alpha < 1$  consists of an interface between water and vapor. In the VOF model, the sum of the volume fractions of all phases in each control volume is equal to one. In the CFD modelling, the Navier–Stokes equations are solved simultaneously. The governing equations involved with the VOF method have been described below. Continuum Surface Force (CSF) model has been adopted to incorporate surface tension effects and added as a source term in the momentum equation [16]. The governing equations involved with the VOF method have been described below.

Continuity:

$$\frac{\delta}{\delta t}(\rho) + \sum_{j=1}^3 \frac{\delta}{\delta x_j}(\rho u_j) = S_M \quad (1)$$

Momentum:

$$\frac{\delta}{\delta t}(\rho u_i) + \sum_{j=1}^3 \frac{\delta}{\delta x_j}(\rho u_i u_j) = -\frac{\delta \rho}{\delta x_i} + \sum_{j=1}^3 \frac{\delta}{\delta x_j} \left[ \mu \left( \frac{\delta u_i}{\delta x_j} + \frac{\delta u_j}{\delta x_i} - \frac{2}{3} \delta_{ij} \sum_{i=1}^3 \frac{\delta u_i}{\delta x_i} \right) \right] + S_{F,j} \quad (2)$$

Energy:

$$\frac{\delta}{\delta t}(\rho E) + \sum_{j=1}^3 \frac{\delta}{\delta x_j}(\rho E u_j) = \sum_{l=1}^3 \sum_{j=1}^3 \left[ \frac{\delta}{\delta x_j}(\tau_{lj}) u_l \right] - \sum_{j=1}^3 \frac{\delta}{\delta x_j} q_j + S_E \quad (3)$$

At this variation of the governing equations the density,  $\rho$ , and the dynamic viscosity,  $\mu$ , of the fluid are presented as functions of the volume fractions of each phase,  $\alpha_K$ , and are defined:

$$\rho = \sum_{K=1}^2 \alpha_K \rho_K \quad (4)$$

$$\mu = \sum_{K=1}^2 \alpha_K \mu_K \quad (5)$$

The VOF numerical approach for modelling multiphase flows is treating the energy,  $E$ , and the temperature,  $T$ , as mass-averaged variables. The energy is defined:

$$E = \frac{\sum_{k=1}^2 \alpha_k \rho_k E_k}{\sum_{k=1}^2 \alpha_k \rho_k} \quad (6)$$

where  $E_k$  for each phase depends on the interaction of the specific heat and the temperature fields of the individual phases. The continuity of  $\alpha$  is carried through an interface mass balance, depicted by the following equation:

$$\frac{\delta \alpha}{\delta t} + u \nabla \alpha = 0 \quad (7)$$

When  $\alpha = 1$ , the whole volume of the computational domain is occupied by the gas phase. In the case when  $\alpha = 0$ , the whole volume is occupied by the liquid phase. The interface (contact) regions between the two phases were formed in the areas where  $\alpha = 0-1$ . When the temperature of the liquid phase exceeds the saturation temperature  $T_{sat}$ , a component with the mass rate of  $S_M$  transfers from the liquid phase to the vapor phase, during which a certain amount of energy  $E$  is absorbed.

Based on the governing equation described above, in the simulation setting, under the model, the volume of the fraction was selected with the number of Eulerian of 3 indicating air, water, and water vapor. For this system, the flow was assumed to be in laminar. For phase, steam (water vapor) was defined as the primary phase, water (liquid) as the secondary phase, and air as a tertiary phase. The air fraction initially filled the space over the liquid phase, allowing for accurate unsteady modeling of the evaporation process [21].

### 2.5 Boundary condition

Based on Elshamy's [6] experimental work, three different input power of 245 W, 552 W and 984 W were used. Here in the simulation setting, different values of heat flux of 8 203.65, 18 483.32 and 32 948.53 W/m<sup>2</sup> were applied at the evaporator wall. For the adiabatic wall, heat flux was set as zero. While, at the condenser wall, a constant temperature of 298 K was applied for all cases. Each wall was imposed with a non-slip boundary condition [21][23]. At the general setup, gravitational acceleration of - 9.81 m/s<sup>2</sup> was set at a positive y-axis direction. This indicates that the thermosyphon relies on gravity for condensate to return from the condenser section back into the evaporator section. Under the mass, heat and reaction in phase interaction, the number of mass mechanisms was set to one for phase interaction from water (liquid) into water (vapor). The evaporation-condensation model was selected, and saturation temperature was changed to 321 K. Then, pressure in the operating condition section was set to 11000 Pa, for water to boil at lower temperature from normal boiling point, pressure applied into the system was reduced. While at initialization state, the temperature was set to 300 K when water volume fraction and air volume fraction equal zero. At initialization, the fill ratio was set up by patching the water at a volume fraction equal to one in the evaporator section and air was patched at a volume fraction equal to zero at the entire fluid domain in the system.

### 2.6 Solution and convergence condition

In this case, a transient simulation was carried out to simulate the dynamic behaviour of the two-phase flow between gas-liquid phases. For the volume of fluid (VOF) model, the global Courant number must be below 250 [12] [17]. Hence, a smaller time step needed to be used to avoid divergence. For this simulation, the time step was set to 0.005 seconds. Under the solution, the method for pressure-velocity coupling was set as SIMPLE. Geo- Reconstruct and PRESTO discretization were selected for volume fraction and pressure interpolation scheme. [12] [17] Under the monitor section of the solution, for the numerical computation to be considered converged, the scaled residual of the mass and velocity component was set to 10<sup>-3</sup> while the energy was set to 10<sup>-4</sup>.

## 3. Result and Discussion

### 3.1 Model validation

From the simulation conducted, temperature distribution at the outer surface of the thermosyphon was recorded after 60 seconds and presented in the form of the graph as shown in Figures (3,4 and 5). A comparison of temperature distribution between the experimental data from Elshamy [6] was tabulated as shown in Table 4, and percentage error was calculated.

The data was taken at the length of the thermosyphon between 0.55 m and 0.8 m. Length of 0.55 to 0.6 m represent the evaporator section, while between 0.6 m to 0.8 m represent the adiabatic

section. During the boiling process, phase change was significantly detected between the evaporator and adiabatic sections because heat and mass transfer occurred between the system's interphase of water and air. Based on Table 4, most of the CFD predicted data were higher than the experimental data. The average percentage error for the power input of 245 W, 552 W, and 984 W were 1.70 %, 2.5 %, and 2.50%, respectively. Mechanical losses caused these errors during the experiment, as described by Elshamy [6] which caused the temperature to become lower.

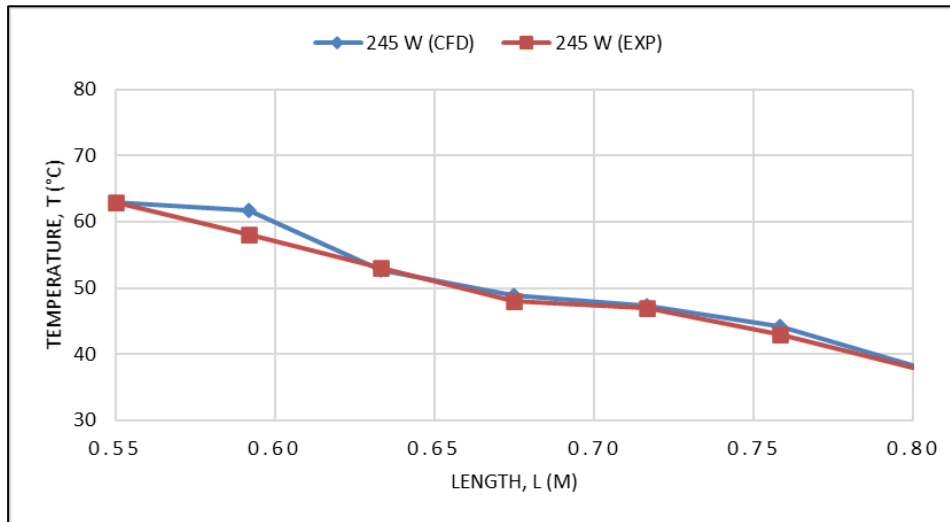


**Fig. 3.** Comparison of temperature distribution at the outer surface of the thermosyphon (P=245 W)

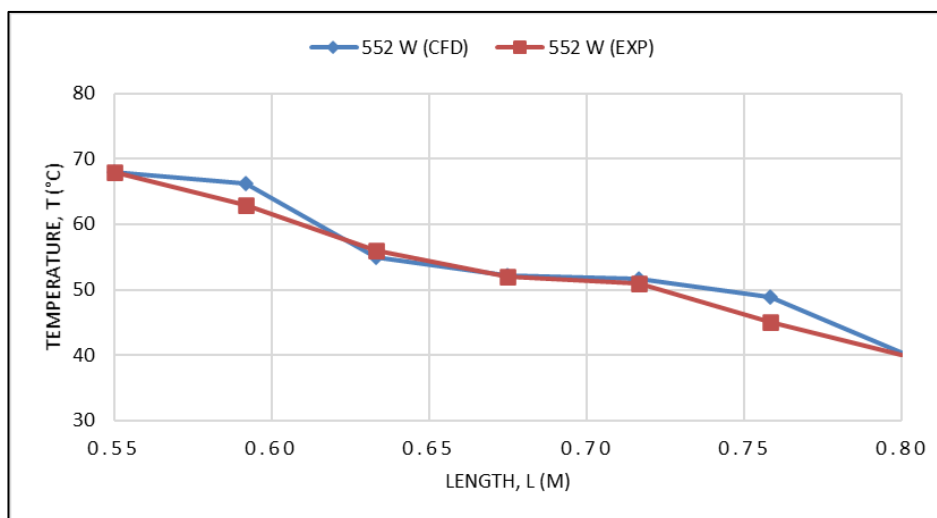


**Fig. 4.** Comparison of temperature distribution at the outer surface of the thermosyphon (P=552 W)

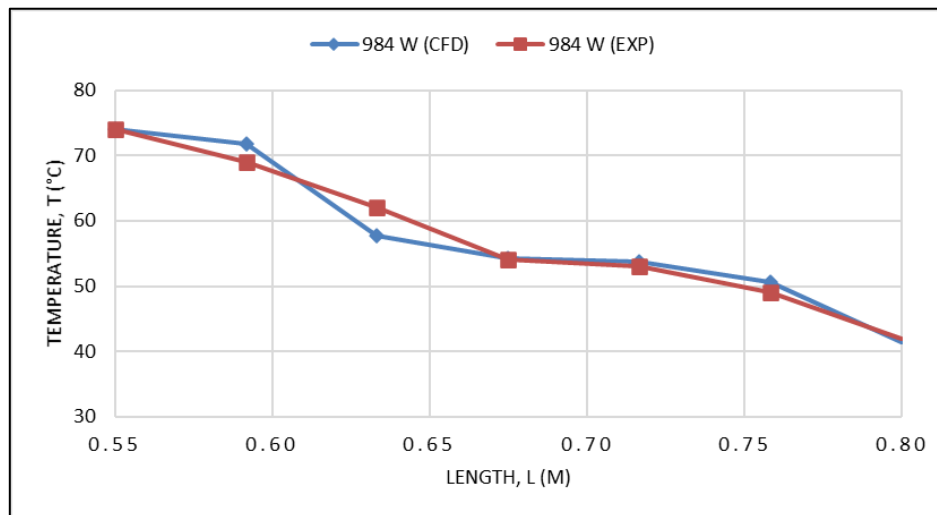


**Fig. 5.** Comparison of temperature distribution at the outer surface of the thermosyphon (P=984 W)

**Table 4**

Comparison between experimental and CFD predicted data for different power inputs

Power input = 245 W			Power input = 552 W			Power input = 984 W		
Temperature (°C)		Error (%)	Temperature (°C)		Error (%)	Temperature (°C)		Error (%)
EXP	CFD		EXP	CFD		EXP	CFD	
63	63.00	0.00	68	68.00	0.01	74	73.99	0.01
58	61.70	6.05	63	66.23	4.87	69	71.78	3.87
53	52.76	0.45	56	55.02	1.78	62	57.78	7.30
48	48.83	1.70	52	52.22	0.42	54	54.28	0.52
47	47.26	0.54	51	51.73	1.40	53	53.7	1.30
43	44.11	2.52	45	48.91	8.00	49	50.65	3.26
38	38.25	0.65	40	40.40	0.99	42	41.43	1.38
Average error %		1.70	Average error %		2.50	Average error %		2.52

### 3.2 Evaporation and condensation processes

To describe more about the phase change that occurred inside the thermosyphon, water volume fraction and temperature contour for the different input power were presented below. From the water volume fraction contour, the red color represents the water volume fraction is 1, which means only water was present. While the blue color indicates that the air volume fraction equals 0, which means no air was present. As shown in Figure 6, at the initial state, at 0 s, the water was filling up the evaporator section.

As heat flux was inputted at the evaporator wall, the heat was transferred into the water through the wall of the evaporator section. As the heating process continued, tiny vapor bubbles started to appear in the water and rose to the interphase between the water vapor phase as shown at 5 seconds during the boiling process. The bubble form or vapor molecules started to appear as shown at 5 seconds. However, up until 60 seconds, nucleate boiling was seen at the interphase between the water and vapor phase. This happened because the surface temperature was hotter than the saturated fluid temperature by 15 °C. At the nucleation side, the formed water vapor showed the vigorous movement of water flow due to vapor bubbles that broke off to the vapor phase at the interphase. But, at 60 seconds, the simulation could not simulate the bulk vapor bubbles at the adiabatic and condenser section. Hereby shows that the in-built evaporation-condensation

model developed by Lee managed to simulate the boiling phenomena inside the system but was unable to visualize the flow of vapor as it fills up the whole thermosyphon.

The time required by forming continuous vapor bubbles in the system is shortened when heat input was increased. Water volume fraction using the input power of 984 W in Figure 8 showed that at 60 seconds, the flow of water and vapor interphase was more vigorous. Its vapor bubbles were bigger in size compared to Figure 6 and Figure 7.

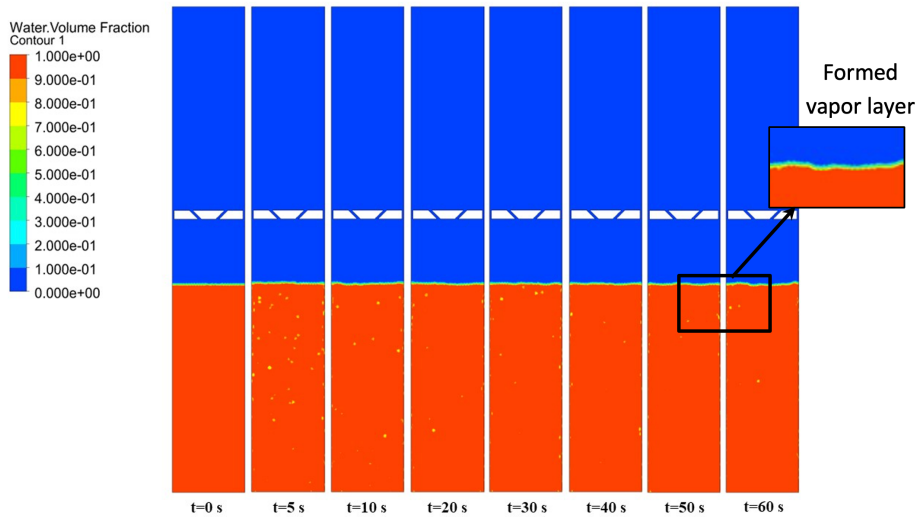


Fig. 6. Water volume fraction (P=245 W)

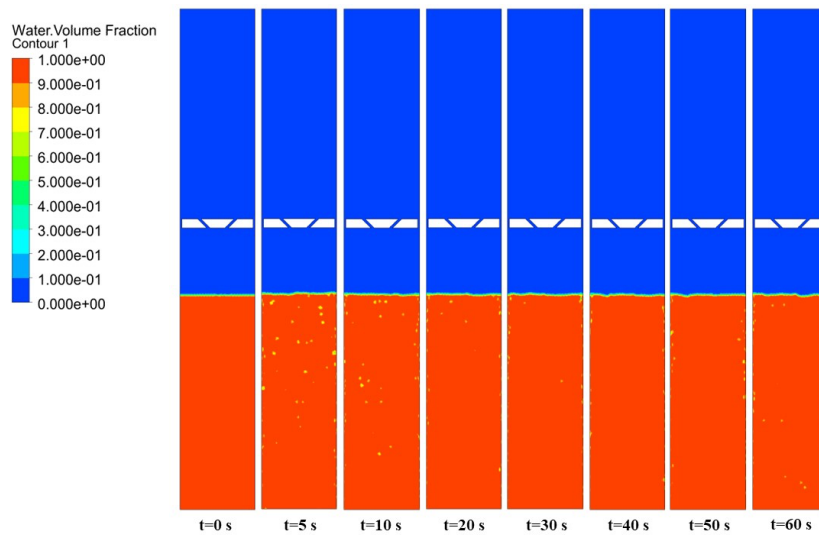
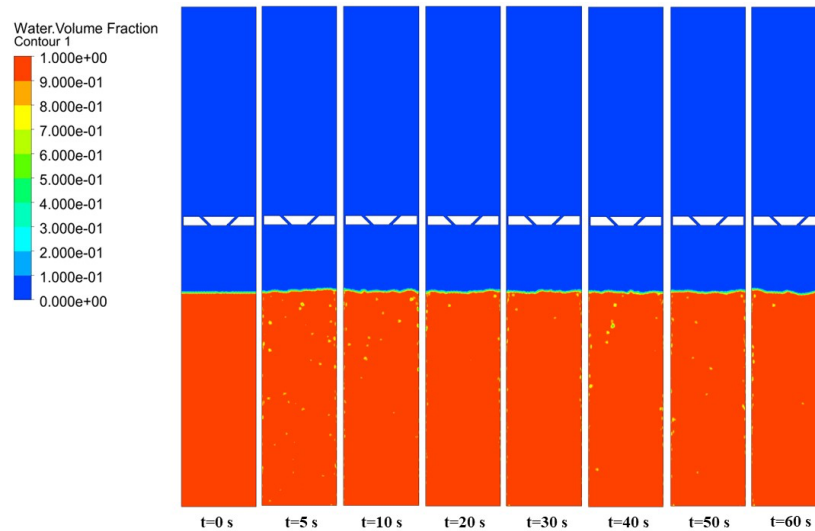


Fig. 7. Water volume fraction (P=552 W)



**Fig. 8.** Water volume fraction (P=984 W)

### 3.3 Temperature distribution

The temperature distribution contour inside the thermosyphon for different heat input cases is shown in Figures (9,10, and 11). At the initial state, the water temperature was set as 300 K, which indicates a real-life situation. In some simulations, the temperature was set to saturation condition to make the entire fluid inside the thermosyphon possess a temperature close to a saturation condition during the initial phase [22].

Based on all case temperature contours, as the heat was inputted through the evaporator wall, the water temperature near the wall and at the interphase side starts to increase by 1°C and the temperature continuously increased from the interphase side to the adiabatic and condenser section. As the time approaches 60 seconds, the water temperature increases to 309 K, and at the interphase between the water and vapor phases, the temperature rapidly rises from 309 K to 321 K, which indicates the surface of evaporation. As a constant temperature of 298 K was set to the condenser wall for condensation to occur, the temperature distribution at the condenser section shows decreasing temperature variation from the centre towards the condenser wall. The vapor will turn into the thin liquid film at the condenser wall, and due to gravitational pull, the condensate will return to the evaporator section. By comparing the temperature at 5 seconds r all cases, the temperature at the centre of the condenser section in Figure 9, Figure 10 and Figure 11 is 313 K, 315 K, and 322 K, respectively. This indicates that as input power increased, the time taken to reach 321 K was shortened.

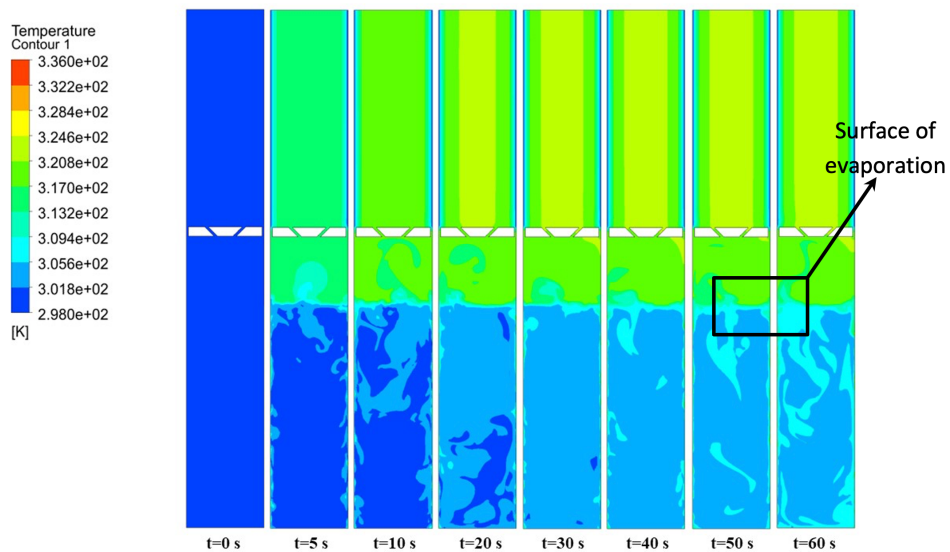


Fig. 9. Temperature contour (P=245 W)

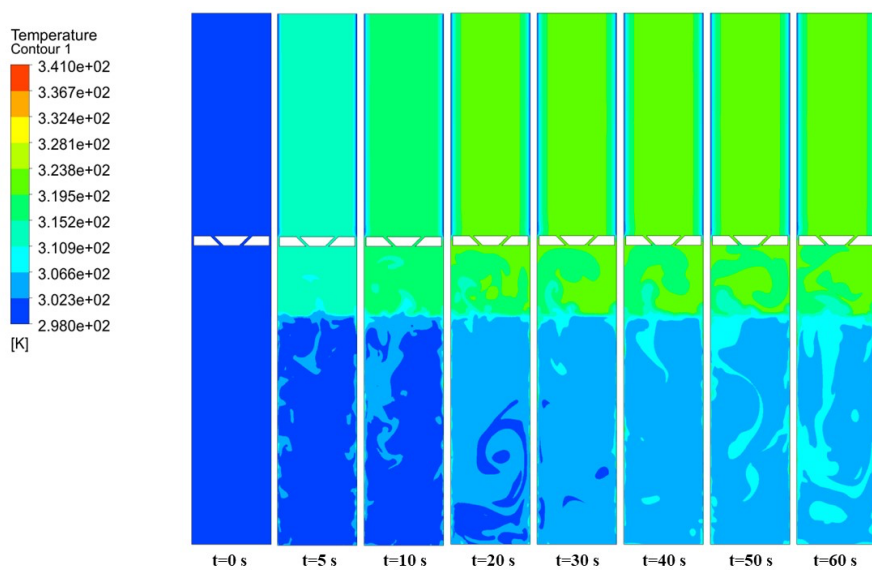
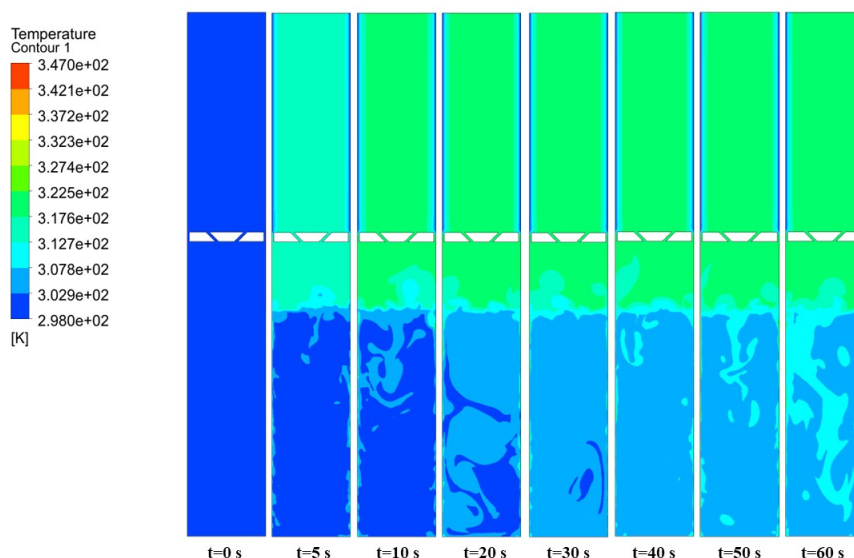


Fig. 10. Temperature contour (P=552 W)



**Fig. 11.** Temperature contour (P=984 W)

### 3.4 Temperature distribution inside the evaporator and adiabatic section

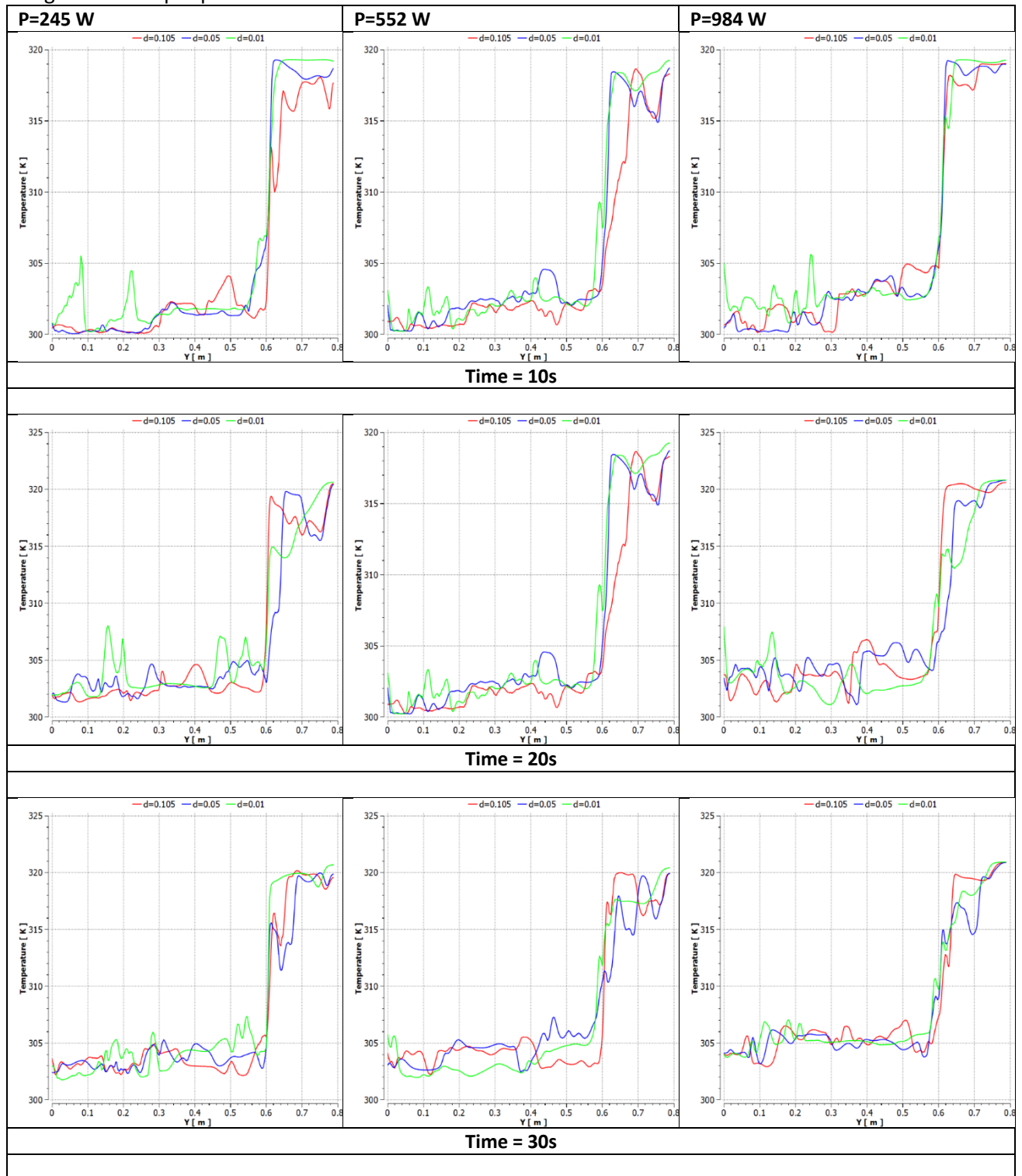
Temperature distribution at the evaporator and adiabatic section is based on the variation of time and distance from the thermosyphon wall as shown in the Table below. The graph of temperature distribution at these sections was recorded every time of 10, 20, 30, 40, 50, and 60 seconds. To evaluate more details, the temperature distributions were also plotted at three variations of distance from the thermosyphon, which were 0.105 m (center location of the thermosyphon), 0.05 m (closer location towards the thermosyphon wall) and 0.01 m (closest location near the thermosyphon wall).

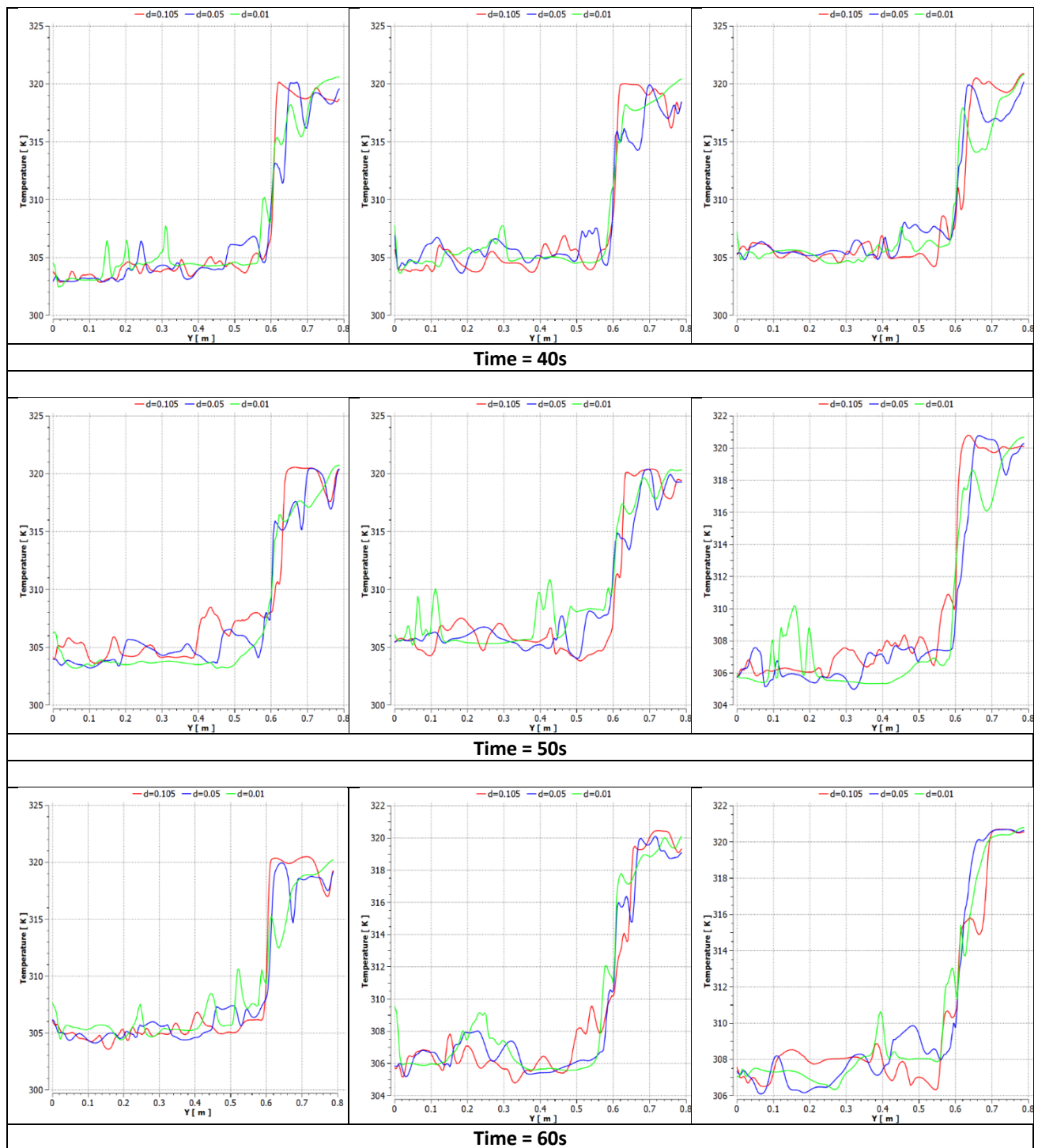
At 10 seconds, for all cases of input power, the temperature at a distance of 0.01 m near the thermosyphon wall was significantly higher than at a distance of 0.105 m (center of the thermosyphon), where the temperature was dropped as the heat was transfer from the wall into the water in the evaporator section. However, the temperature starts to gradually increase when approaching the adiabatic section. Also, in the adiabatic section, the temperature was detected to be almost in constant temperature as there was no heat flux applied in this section.

At 60 seconds, for all cases of input power, the temperature at a distance of 0.01 m near the thermosyphon wall was almost the same as the temperature at a distance of 0.105 m (center of the thermosyphon), which indicates that the system has acquired same temperature distribution all over the system's section. By comparing based on different heat input, the temperature at the adiabatic section at the center of the thermosyphon with using input power of 245 W was 320 K, while using an input power of 552 W was 320 K, and for input power of 984 W was 321 K. Lower input power results in almost similar temperature distribution inside the evaporator section, while higher input power results in slightly higher temperature distribution.

**Table 5**

Comparison of temperature distributions inside the evaporator and adiabatic section at different location using different input power





### 3.5 Velocity and streamline profile

The velocity and streamline distribution inside the thermosyphon for different input power are presented in Figures (12, 13, and 14). A turbine was attached between the adiabatic and condenser section based on the real thermosyphon Rankine engine model. However, in this study, only the thermosyphon model based on the TSR engine design was investigated. Two nozzles existed in the system to allow the air velocity from the vapor to rotate the turbine. Hence, the velocity of vapor plays an essential role in the TSR engine for rotating the turbine.

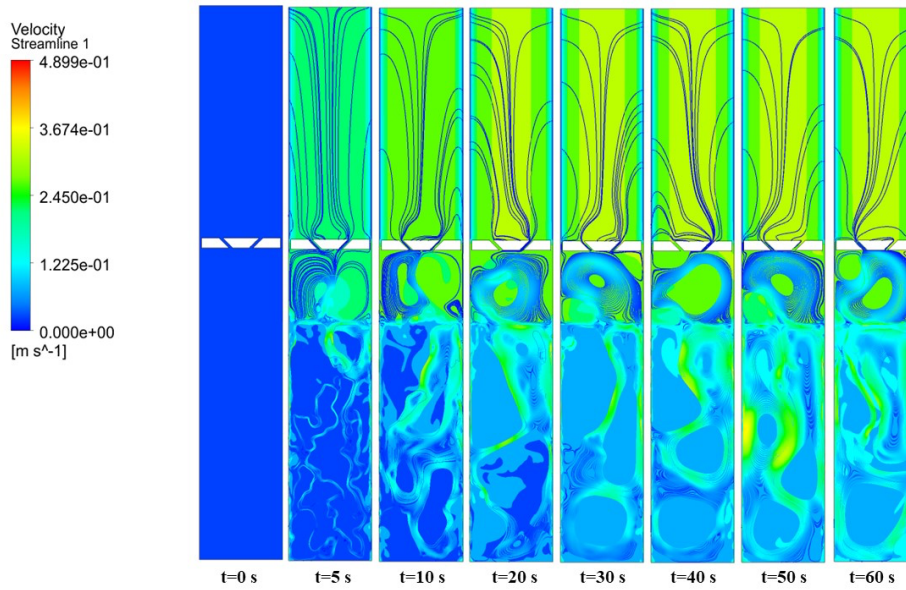


**Fig. 12.** Velocity streamline (P=245 W)

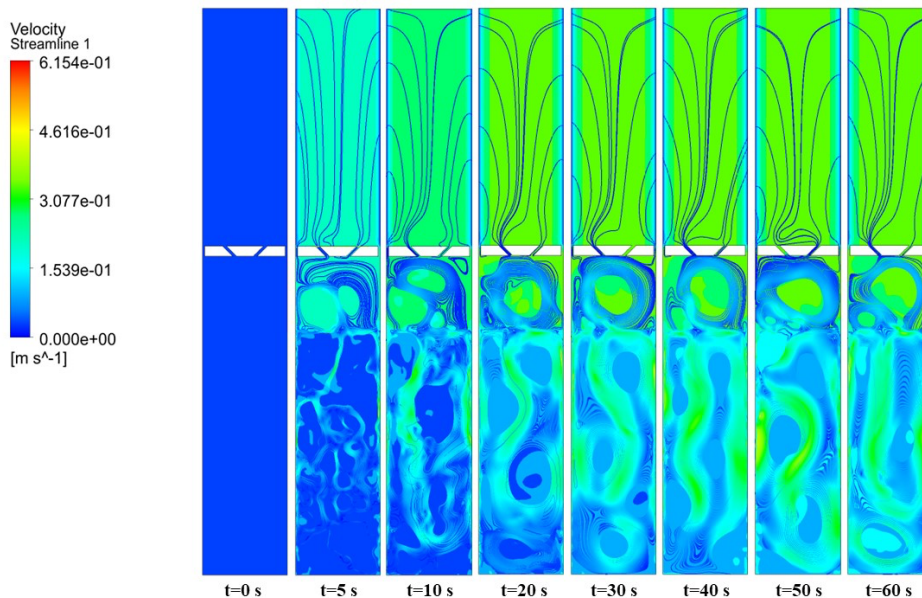


**Fig. 13.** Velocity streamline (P=552 W)

Figure 12, showed that the highest velocity recorded inside the system at 60 seconds was 0.4899 m/s, while in Figure 13, the highest velocity recorded was 0.6154 m/s. In Figure 14, the highest velocity recorded at 60 seconds was 0.6743 m/s and it shows the velocity rose to reach the adiabatic section. This indicates that increasing the heat input can increase the air velocity in the system. Elshamy [6] states that the output power also increases by increasing the input power. However, in his experiment, as output power increases, the system experience decreases efficiency.

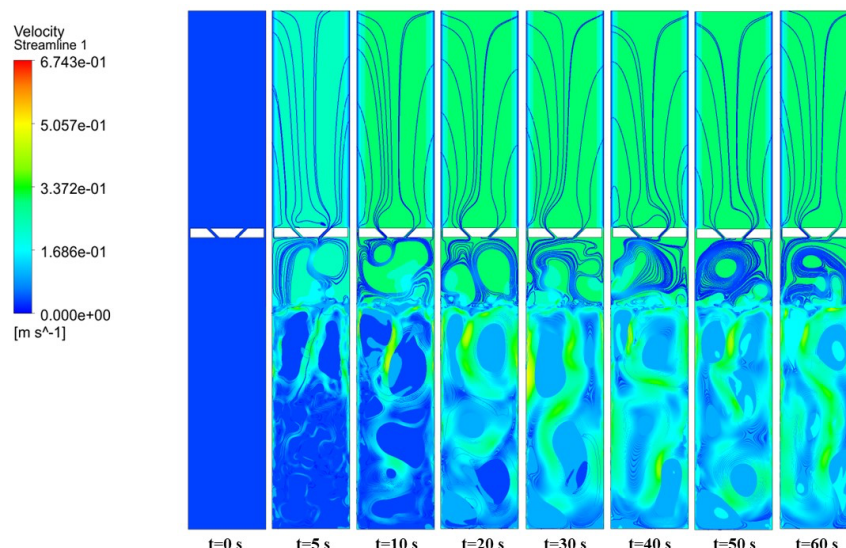


**Fig. 14.** Velocity streamline (P=984 W)

### 3.6 Velocity at the outlet area of the nozzle

For more details on velocity profile inside the system, velocity profile at the outlet area of the nozzle based on time and different input power were presented in Table form. From the Table, a comparison of the velocity for the left and right nozzle were plotted as shown in Figure.

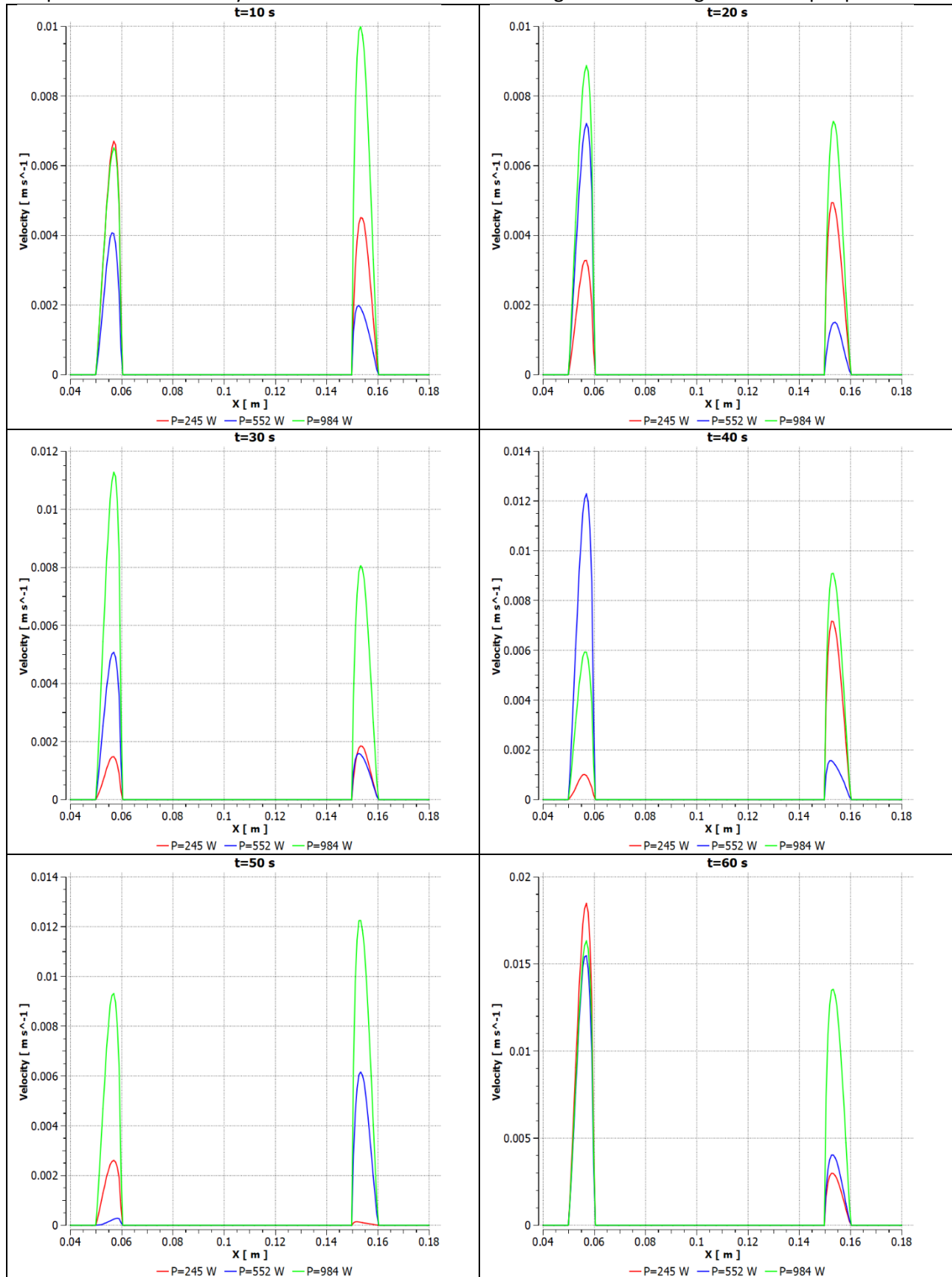
Based on Figure 15, from an input power of 245 W, the peak velocity at 10 seconds was 0.00675 m/s. Then the velocity was dropped as time increased, and at 50 seconds, the velocity rose up to 0.0185 m/s. While for input power of 552 W, the peak velocity at 10 seconds was 0.0041 m/s, then keep increased and dropped after 20 seconds, but increased again after 30 seconds and decreased after 40 seconds, finally rose to 0.0155 m/s after 50 seconds. While for input power of 984 W, the peak velocity at 10 seconds was 0.00672 m/s, then keep increased and dropped after 30 seconds, but rose again after 40 seconds to 0.0165 m/s at 60 seconds.

For Figure 16, for input power of 245 W, the peak velocity at 10 seconds was 0.0045 m/s, then dropped after 20 seconds, but increased again after 30 seconds and decreased after 40 seconds, finally rose to 0.003 m/s at 60 seconds. While for input power of 552 W, the peak velocity at 10 seconds was 0.002 m/s, started to increase at 40 seconds, and dropped to 0.004 m/s. While, for input power of 984 W, the peak velocity at 10 seconds 0.01 m/s, then decreased and rose up after 20 seconds to 0.01375 m/s at 60 seconds.

From the trend, the peak velocity was in an irregular pattern for every case, either the right or left nozzle. However, the trend of the peak velocity using the higher input power results in a minor deviation between each velocity at different times. Compared to others, the trend of the peak velocity for input power of 984 W was higher in the range. This indicates that using higher input power can results in the constant of high velocity for the system to rotate the turbine at higher rotational rate.

**Table 6**

Comparison of the velocity at the outlet area of the left and right nozzles using different input power



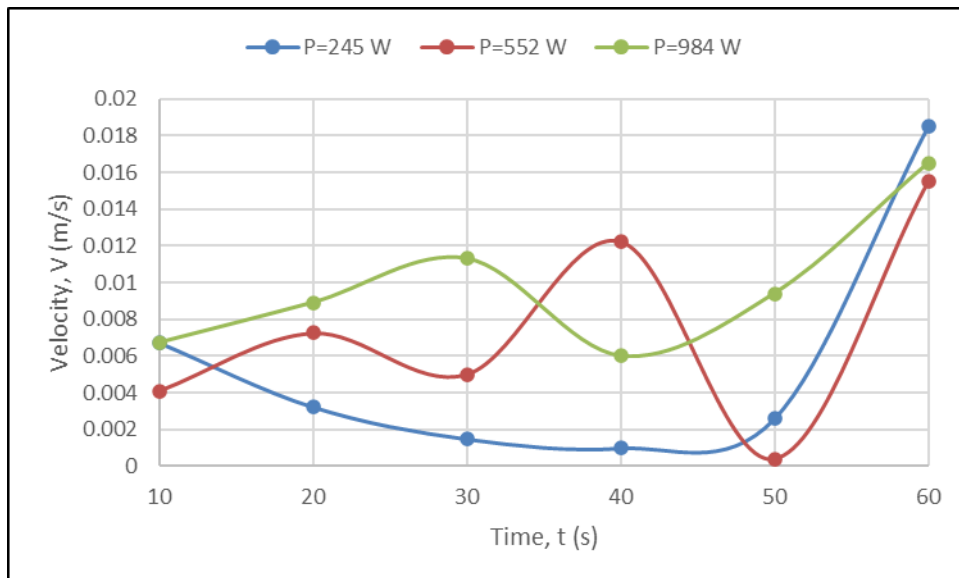


**Fig. 15.** Comparison of the peak velocity at the outlet area of the left nozzle using different input power

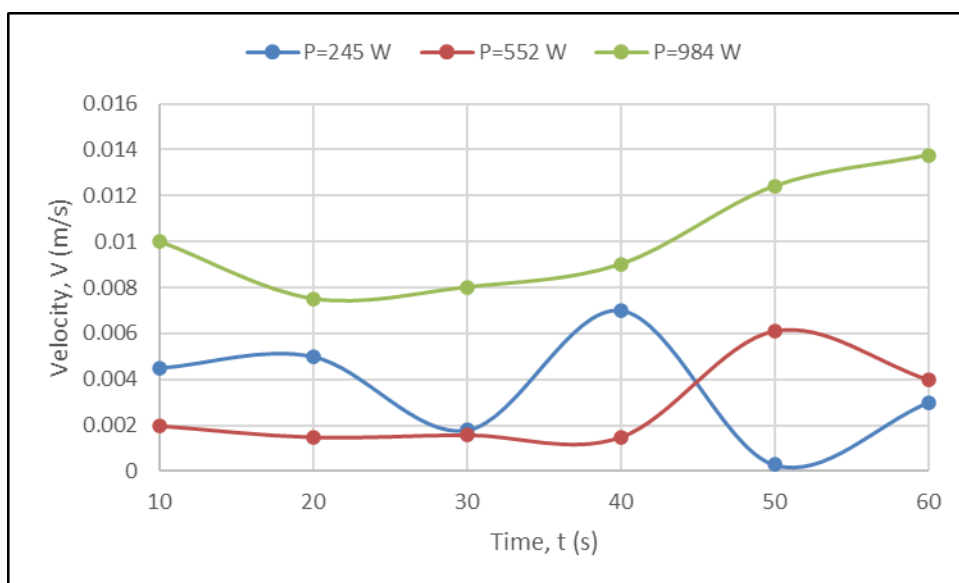


**Fig. 16.** Comparison of the peak velocity at the outlet area of the right nozzle using different input power

#### 4. Conclusion

The application of thermosyphon coupled with available low heat resources, especially thermosyphon Rankine energy, was not quite well known in our society. Many researchers have applied the utilization of thermosyphon on the other hand for finding the optimum design of the system to increase the system's performance.

In this paper, the CFD simulation approach was done on the thermosyphon based on the specification of the thermosyphon Rankine engine model developed by Elshamy in his experimental work. ANSYS FLUENT software version 2020 R2 was used to simulate the gas-liquid phase's two-phase flow during the evaporation and condensation processes with different input power, using the

Volume of Fluid (VOF) method with in-built evaporation-condensation model by Lee applicable in Fluent. 2D geometry of thermosyphon was created to reduce the computational time for the simulation.

Temperature distribution along the outer surface was recorded and compared with experimental data from the simulation. The simulation data was higher than the experimental one due to mechanical losses during experimentation based on the comparison. As for visualization, the model simulated the vapor bubbles and nucleate boiling at the interphase between water and gas through water volume fraction contour. As for the temperature distribution inside the thermosyphon was higher at the centre of the condenser section than at the evaporator, but near the condenser wall, the temperature dropped, indicating condensation. The result shows that the VOF model with in-built evaporation-condensation model managed to simulate vapor bubbles and vapor layer at the interphase well during the boiling process. However, it was limited to visualize the entire vapor volume fraction and condensation liquid film more time iteration needed to be done to capture it. However, the model was able to simulate the temperature distribution well.

In the future, the ANSYS FLUENT should be created with complete heat and mass transfer mechanisms in the evaporation-condensation model to be coupled with the VOF model. According to previous research, many utilized user-defined function codes in Fluent to simulate the complete evaporation and condensation model. However, studies in UDF code were not well known by many, and it was hard to understand for minors and beginners. Instead of having external code to fulfill the simulation process, the software should be implemented with complete code for evaporation and condensation.

## References

- [1] Zhang, Tiantian, and Hongxing Yang. "High efficiency plants and building integrated renewable energy systems: Building-integrated photovoltaics (BIPV)." *Handbook of Energy Efficiency in Buildings: A Life Cycle Approach*; Elsevier: Amsterdam, The Netherlands (2018): 441-595. <https://doi.org/10.1016/B978-0-12-812817-6.00040-1>
- [2] Yoon, Jongseung, Yugang Sun, and John A. Rogers. "Flexible solar cells made of nanowires/microwires." In *Semiconductor Nanomaterials for Flexible Technologies*, pp. 159-196. William Andrew Publishing, 2010. <https://doi.org/10.1016/B978-1-4377-7823-6.00006-4>
- [3] Chauhan, Rajeev Kumar, and Kalpana Chauhan, eds. *Distributed energy resources in microgrids: integration, challenges and optimization*. Academic Press, 2019.
- [4] Lund, Henrik. "Renewable energy strategies for sustainable development." *energy* 32, no. 6 (2007): 912-919. <https://doi.org/10.1016/j.energy.2006.10.017>
- [5] Jouhara, Hussam, Amisha Chauhan, Theodora Nannou, S. Almahmoud, Bertrand Delpech, and Luiz C. Wrobel. "Heat pipe based systems-Advances and applications." *Energy* 128 (2017): 729-754. <https://doi.org/10.1016/j.energy.2017.04.028>
- [6] Elshamy, Samir M. "Performance of Thermosyphon Rankine Engine as Low Temperature Heat Engine." *International Journal of Scientific & Engineering Research* (2017): 126-130.
- [7] Habieeb, Abed Rabiee, Gamal Ebrahim Sultan, Mohamed Mahmoud Awad, and Ahmed Refaat Elshamouty. "An Experimental Study of a Two-Phase Closed Thermosyphon Rankine Cycle Performance." *MEJ. Mansoura Engineering Journal* 45, no. 1 (2020): 21-30. <https://doi.org/10.21608/bfemu.2020.89188>
- [8] Ziapour, B. M., A. Mohammadnia, and M. Baygan. "More about Thermosyphone Rankine Cycle Performance Enhancement." *International Journal of Engineering* 28 (2015): 642-647. <https://doi.org/10.5829/idosi.ije.2015.28.04a.20>
- [9] Saadon, Syamimi, and Nur Athirah Mohd Nasir. "Modelling and Thermal Analysis of Organic Rankine Cycle with Superheater and Preheater." *Journal of Advanced Research in Fluid Mechanics and Thermal Sciences* 55, no. 2 (2019): 142-149.
- [10] Islam, Salmah Md Saiful, and Syamimi Saadon. "Performance Analysis of Supercritical Organic Rankine Cycle System with Different Heat Exchangers Design Configuration." *Journal of Advanced Research in Fluid Mechanics and Thermal Sciences* 65, no. 2 (2020): 324-333.
- [11] Touaibi, Rabah, Hasan Köten, Michel Feidt, and Ozlem Boydak. "Investigation of three organic fluids effects on exergy analysis of a combined cycle: organic Rankine cycle/vapor compression refrigeration." *Journal of Advanced*

- Research in Fluid Mechanics and Thermal Sciences* 52, no. 2 (2018): 232-245.
- [12] Alizadehdakheel, Asghar, Masoud Rahimi, and Ammar Abdulaziz Alsairafi. "CFD modeling of flow and heat transfer in a thermosyphon." *International Communications in Heat and Mass Transfer* 37, no. 3 (2010): 312-318. <https://doi.org/10.1016/j.icheatmasstransfer.2009.09.002>
- [13] Yang, K. M., Z. Cong, and W. F. Wang. "CFD simulation of flow and heat transfer in a thermosyphon." In *Sustainable Development: Proceedings of the 2015 International Conference on Sustainable Development (ICS2015)*, pp. 1038-1044. 2016. [https://doi.org/10.1142/9789814749916\\_0110](https://doi.org/10.1142/9789814749916_0110)
- [14] Fadhl, B., L. C. Wrobel, and H. Jouhara. "Modelling of the thermal behaviour of heat pipes." *WIT Transactions on Engineering Sciences* 83 (2014): 377-389. <https://doi.org/10.2495/HT140331>
- [15] Fadhl, Bandar, Luiz C. Wrobel, and Hussam Jouhara. "CFD modelling of a two-phase closed thermosyphon charged with R134a and R404a." *Applied Thermal Engineering* 78 (2015): 482-490. <https://doi.org/10.1016/j.applthermaleng.2014.12.062>
- [16] Bouhal, T., Y. Agrouaz, T. Kousksou, T. El Rhafiki, and Y. Zeraoui. "Performance optimization of a two-phase closed thermosyphon through CFD numerical simulations." *Applied Thermal Engineering* 128 (2018): 551-563. <https://doi.org/10.1016/j.applthermaleng.2017.09.049>
- [17] Fadhl, Bandar, Luiz C. Wrobel, and Hussam Jouhara. "Numerical modelling of the temperature distribution in a two-phase closed thermosyphon." *Applied Thermal Engineering* 60, no. 1-2 (2013): 122-131. <https://doi.org/10.1016/j.applthermaleng.2013.06.044>
- [18] Wang, Xiaoyuan, Yinfeng Wang, Haijun Chen, and Yuezhaoh Zhu. "A combined CFD/visualization investigation of heat transfer behaviors during geyser boiling in two-phase closed thermosyphon." *International Journal of Heat and Mass Transfer* 121 (2018): 703-714. <https://doi.org/10.1016/j.ijheatmasstransfer.2018.01.005>
- [19] Wang, Yinfeng, Xiaoyuan Wang, Haijun Chen, Robert A. Taylor, and Yuezhaoh Zhu. "A combined CFD/visualized investigation of two-phase heat and mass transfer inside a horizontal loop thermosiphon." *International Journal of Heat and Mass Transfer* 112 (2017): 607-619. <https://doi.org/10.1016/j.ijheatmasstransfer.2017.04.132>
- [20] Temimy, Alaa AB, and Adnan A. Abdulrasool. "CFD Modelling for flow and heat transfer in a closed Thermosyphon charged with water—A new observation for the two phase interaction." In *IOP Conference Series: Materials Science and Engineering*, vol. 518, no. 3, p. 032053. IOP Publishing, 2019. <https://doi.org/10.1088/1757-899X/518/3/032053>
- [21] Lenhard, Richard, Milan Malcho, and Jozef Jandačka. "Modelling of heat transfer in the evaporator and condenser of the working fluid in the heat pipe." *Heat transfer engineering* 40, no. 3-4 (2019): 215-226. <https://doi.org/10.1080/01457632.2018.1426225>
- [22] Singhal, Sagar, Abhishek Gaikwad, and Jeevan Jaidi. "CFD ANALYSIS OF A WICKLESS HEAT PIPE." In *Proceedings of the 24th National and 2nd International ISHMT-ASTFE Heat and Mass Transfer Conference (IHMTC-2017)*. Begel House Inc., 2017. <https://doi.org/10.1615/IHMTC-2017.2260>
- [23] Song, Hongjie, Wei Zhang, Yaqi Li, Zhengwei Yang, and Anbo Ming. "Simulation of the vapor-liquid two-phase flow of evaporation and condensation." *International Journal of Heat and Technology* 34, no. 4 (2016): 663-670. <https://doi.org/10.18280/ijht.340416>